AIP Advances

Signal-to-noise ratio enhanced electrode configurations for magnetoelectric cantilever sensors EP

Julius Schmalz, Matthias C. Krantz, Alexander Knies, et al.

COLLECTIONS

EP   This paper was selected as an Editor's Pick

View Online   Export Citation   CrossMark

ARTICLES YOU MAY BE INTERESTED IN

Magnetoelectric cantilever sensors under inhomogeneous magnetic field excitation
AIP Advances **10**, 025132 (2020); https://doi.org/10.1063/1.5136239

Effect of excitation mode on the magnetic field detection limit of magnetoelectric composite cantilevers
AIP Advances **10**, 045108 (2020); https://doi.org/10.1063/1.5138639

Deep learning surrogate model for kinetic Landau-fluid closure with collision
AIP Advances **10**, 075108 (2020); https://doi.org/10.1063/5.0010917

Signal-to-noise ratio enhanced electrode configurations for magnetoelectric cantilever sensors EP

View Online   Export Citation   CrossMark

Julius Schmalz,[a] iD **Matthias C. Krantz, Alexander Knies, Hannes Lüder,** iD **and Martina Gerken** iD

AFFILIATIONS

Faculty of Engineering, Kiel University, Kaiserstraße 2, 24143 Kiel, Germany

[a]Author to whom correspondence should be addressed: jusc@tf.uni-kiel.de

ABSTRACT

Magnetoelectric cantilevers consisting of strain-coupled magnetostrictive and piezoelectric (PE) layers are applicable to magnetic-field sensing. For the first bending mode, the magnetic field-induced stress distribution is of equal sign along the cantilever length. Thus, a plate-capacitor electrode configuration encompassing the complete PE layer may be used for collecting the strain-induced charge. For higher order modes, stress regions of the opposite sign occur in the cantilever length direction. To prevent charge cancellation and to harvest the piezo-electric induced charge efficiently, segmented electrodes are employed. This study investigates the effect of the electrode configuration on the signal-to-noise ratio (SNR) for higher order bending modes. The charges collected by the electrodes are calculated using a finite element method simulation considering the mechanical, electrical, and magnetic properties of the cantilever. By combination with an analytic noise model, taking into account the sensor and amplifier noise sources, the SNR is obtained. We analyze a 3 mm long, 1 mm wide, and 50 μm thick silicon cantilever with layers of 2 μm magnetostrictive soft amorphous metal (FeCoSiB) and 2 μm piezoelectric aluminum nitride. We demonstrate that an SNR-optimized electrode design yields an SNR improvement by 2.3 dB and 2.4 dB for the second and third bending modes compared to a signal optimized design.

I. INTRODUCTION

Magnetoelectric (ME) cantilevers are employed for energy harvesting,[1,2] as well as for measuring magnetic fields at room-temperature.[3–5] In both cases, a magnetostrictive (MS) layer and a piezoelectric (PE) layer are used for the conversion of a magnetic field to an induced electric charge by strain coupling of the two layers—with or without an additional substrate. Due to an applied magnetic field, the magnetostrictive layer is deformed. The cantilever and, thus, also the piezoelectric layer are deflected. This deformation causes a change in the polarization and results in a surface charge on the piezoelectric layer. A schematic representation of cantilevers operated in the first three bending modes and the induced charge distributions are depicted in Fig. 1.

For operation at higher modes and for multi-mode operation, the stress distribution along the cantilever is essential for the

electrode design. The common approach is to use a strain-node optimized electrode configuration[6,7] using electrodes segmented at the zeros of the strain distribution along the cantilever. Otherwise, the charge signal is partially canceled by the polarity change. In Zabel et al.,[7] the electrode start and end positions are estimated based on the calculated strain nodes. The estimated positions are compared to a sensitivity optimization based on the Euler–Bernoulli beam theory. We previously demonstrated that an electrode with optimal length for the first bending mode should not cover the entire cantilever.[8] Here, we present a finite-element method (FEM) simulation based study, analyzing the influence of the electrode design on the signal-to-noise ratio (SNR) for the first three bending modes. The sensor is operated in direct detection with a longitudinal applied magnetic field (Fig. 1). In contrast to previous studies on electrode designs for higher order modes,[6,7] we design the electrode configuration for maximum SNR instead of sensitivity. This leads to improved
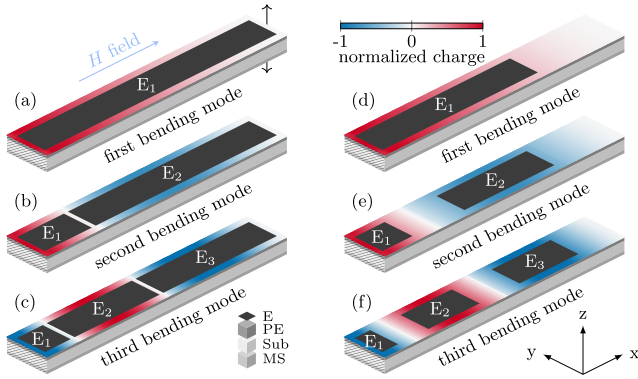
FIG. 1. Strain-node optimized electrode designs for the first three bound-free bending modes on top of a cantilever (a)–(c), as well as SNR optimized electrode designs (d)–(f). The cantilevers consist of a silicon substrate (Sub) sandwiched between a magnetostrictive layer (below) and a piezoelectric layer (above) covered by the electrodes (E) E_1–E_3. The fixed end on the left is hatched, and the cantilever deflection is indicated with black arrows. The piezoelectrically induced surface charge density for the first three bending modes is color-coded on top of the cantilever for an applied magnetic field (H field).

geometries providing higher SNR. In the first part of this study, a FEM model was implemented for the calculation of the signal strength for higher order bending modes. This model, considering the mechanical, electrical, and magnetic properties of the composite cantilever, was verified by experimental results obtained with 45 mm long and 5 mm wide silicon cantilevers with poly(vinylidene fluoride-co-trifluoroethylene) [P(VDF–TrFE)] as a piezoelectric and Metglas as a magnetostrictive layer [Figs. 1(a)–1(c)]. Varying the electrode design and comparing simulation and measurement is particularly well suited to validate the model because the active layers can be kept unchanged, which reduces the influence of fabrication variations.

In the second part of the study, we combined the FEM model for signal strength calculation with an analytic noise model[9] to calculate the SNR. A study investigating the influence of the electrode configuration on the SNR is presented. Using the verified FEM model, the strain node positions for different cantilever dimensions and material properties can be calculated for various electrode configurations. Here, 3 mm long and 1 mm wide silicon cantilevers with active layers of aluminum nitride (AlN) and Metglas were investigated, as these cantilevers were shown to exhibit a particularly low limit of detection for magnetic-field sensing[10] compared to the one chosen for model verification.

II. FINITE-ELEMENT-METHOD MODEL

The coupled mechanical, electric, and magnetic behavior of the magnetoelectric cantilevers were modeled by the coupled differential equation system consisting of Newton's law and Maxwell's equations as follows:[8,11]

$$\nabla \cdot \boldsymbol{T} = -\rho \omega^2 \vec{u}, \tag{1}$$

$$\nabla \cdot \vec{D} = 0, \tag{2}$$

$$\nabla \cdot \vec{B} = 0, \tag{3}$$

where $\boldsymbol{T}$ is the stress tensor, ρ is the mass density, ω is the angular frequency, $\vec{u}$ is the displacement vector, and $\vec{D}, \vec{B}$ is the electric and magnetic flux density. Here, it is assumed that space charges and conduction currents are negligible.

A linearized set of constitutive material equations is evaluated at the small-signal operating point,

$$\boldsymbol{T} = \boldsymbol{c}^{EH}\boldsymbol{S} - \boldsymbol{e}_e\vec{E} - \boldsymbol{e}_m^\top\vec{H}, \tag{4}$$

$$\vec{D} = \boldsymbol{e}_e\boldsymbol{S} + \boldsymbol{\varepsilon}\vec{E}, \tag{5}$$

$$\vec{B} = \boldsymbol{e}_m\boldsymbol{S} + \boldsymbol{\mu}\vec{H}, \tag{6}$$

where $\boldsymbol{S}$ describes the strain tensor, $\boldsymbol{c}^{EH}$ is the stiffness tensor, $\boldsymbol{e}_e$ and $\boldsymbol{e}_m$ are the strain to field coupling constants, $\vec{E}, \vec{H}$ are the electric and magnetic fields, $\boldsymbol{\varepsilon}$ and $\boldsymbol{\mu}$ are the permittivity and permeability, V is the electric potential, and V_m is the magnetic potential.

The elasticity relation is given by Eq. (7) and scalar potentials are assumed for the electric and the magnetic fields [Eqs. (8) and (9)] as

$$\boldsymbol{S} = 1/2\left[(\nabla\vec{u})^\top + \nabla\vec{u}\right], \tag{7}$$

$$\vec{E} = -\nabla V, \tag{8}$$

$$\vec{H} = -\nabla V_m. \tag{9}$$

A 3D simulation of the ME-sensor was performed using COMSOL Multiphysics® implementing the above linear equations in the general form partial differential equation (PDE) interface as a small-signal approximation. The resonance frequency, the stress distribution, and the electrical voltage of the piezoelectric layer were calculated for a magnetic excitation applying an external magnetic flux density of 1 µT at the front and back side of the cantilever in a frequency domain study using these equations. The used material parameters are given in the Appendix.

III. VALIDATION OF THE FEM MODEL

The position of the strain nodes is highly dependent on the sensor dimensions, layer thicknesses, and material properties. For accurate electrode design development, the used FEM model including the material parameters is validated against measurements from in-house fabricated ME sensors. For this, a 45 mm long and 5 mm wide cantilever sensor with 300 µm thick silicon substrate, 2.5 µm thick PVDF–TrFE as a piezoelectric layer, and 29 µm Metglas as a magnetostrictive layer was chosen. The positions of the electrode segmentations were obtained by the strain node positions. Multiple sensors were fabricated with electrodes segmented at the strain nodes of the first, second, and third mode. Here, we focus on the third mode, as the effect of the segmented electrodes on the collected charges is most pronounced. A sensor with an electrode configuration as shown in Fig. 1(c) was chosen as an example with the electrodes segmented at 13.2% and 49.7% of the cantilever length.

A. Fabrication

We fabricated the ME sensors using a 300 µm thick 4-in. silicon wafer from Silicon Materials (Si-Mat). After evaporating a 200 nm

thick aluminum electrode on top of the wafer, the aluminum surface was treated with water dissociation[12] and oxygen plasma for 5 min with 8 sccm O_2 flow and a power of 150 W. This surface treatment was necessary because fluorocarbons are hydrophobic and the adhesion to the metal surface was too weak to get a uniform layer of the PVDF–TrFE used as a PE layer. The polymer solution was prepared by dissolving 1 g P(VDF-TrFE) powder from Piezotech S.A.S. consisting of 70% PVDF and 30% TrFE in 5 ml 4-methyl-2-pentanone and 5 ml 2-butanone. The solution was stirred for 24 h at 600 rpm. 5 ml of this solution was spin-coated onto the aluminum layer with a ramp up time of 6 s, a spinning time of 40 s at 1600 rpm, and a ramp down time of 4 s. After spin-coating, the layer was annealed at 135 °C for 4 h. This led to a layer thickness of approximately 2.5 μm of PVDF–TrFE. After cutting the wafer into 45 mm × 5 mm beams, a 200 nm thick silver layer was evaporated on top of the PE layer as the upper electrode. The poling of the PVDF–TrFE was performed in steps from 20 V/μm to 100 V/μm at 90 °C for 6 min each. Subsequently, a 29 μm thick Metglas foil (2826 MB from HITACHI Metals Europe GmbH) was glued to the lower side of the substrate as a magnetostrictive (MS) layer using epoxy resin (Epoxy Quick Set, UHU). This thin layer of epoxy was neglected in the calculation. The electrodes were contacted using thin copper wires bonded to each segmented electrode.

B. Measurements

In a first experiment, we measured the strain along the cantilever and especially the positions of the strain nodes for the first three bending modes with an optical laser measurement setup. In a second experiment, we measured the collected charges from sensors with segmented electrodes. The segmented electrodes were designed according to the strain node position of the FEM results for the given sensor geometry, layer thicknesses, and material parameters.

Using an optical setup measuring the laser reflection at different points along the cantilever excited in the bending mode, the positions of the strain nodes can be obtained (Fig. 2). By the parallel
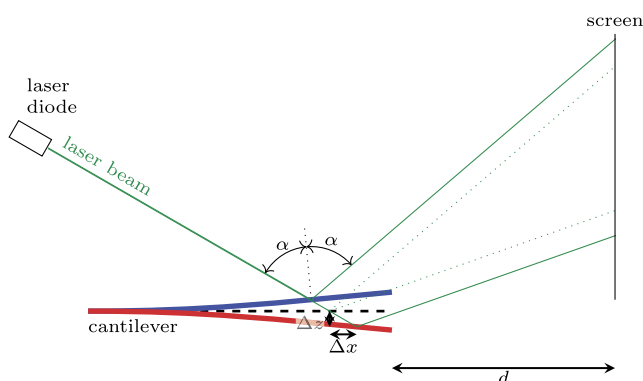
shift of the laser beam, multiple points along the cantilever are measured. During cantilever deflections, the angle of incidence changes continuously producing different reflection pattern amplitudes on the screen. As the laser's incidence angle is dependent on the cantilever slope at the incident point, the reflection pattern amplitude is proportional to the slope of the cantilever displacement $\partial u_z/\partial x$. The distance d between the cantilever and the screen was chosen to ensure that the superposing effect of the reflection point shifting Δx in the x direction and Δz in the z direction can be neglected. The amplitude of the cantilever deflection describing the slope of the displacement along the cantilever for the first three modes is consistent with the FEM results (Fig. 3).

Although the electrodes were designed for a specific mode, the cantilever can be operated at other modes with reduced charge output. The electrical output of the piezoelectric layer was measured under magnetic excitation using a coil [Fig. 4(d)] and a function generator (HAMEG HMFG 2525). The readout of the charges was performed using an AD745 based charge amplifier (Fig. 5). Each electrode was connected to its own charge amplifier for excitation in the first three bending modes. The outputs of the different electrodes are shown in Fig. 4. Unfortunately, the electrode E_2 was shorted during the poling of the PE layer and could not be evaluated. Nevertheless, as our aim was to compare the measurement with the FEM results, a sufficient amount of combinations of modes and electrodes using the two electrodes E_1 and E_3 was measured.

For the readout, each electrode can either be measured separately (labeled E_1 and E_3) or combined (labeled $E_{1,3}$). After analog-to-digital (AD) conversion, the values of the separately measured electrodes are also combined digitally in post-processing. The charges collected by the electrodes were normalized to the electrode with the highest charge.

At the first resonant mode, twice as much charge as on E_3 was observed on E_1. Combining E_1 (1.0) and E_3 (0.5) to $E_{1,3}$ by connecting the two electrodes via a copper wire, the sum of both positive charges was measured (1.51). Adding the AD converted values of each electrode resulted in the same normalized charge as illustrated by the dark blue bar. The same finding was seen for the FEM simulation result.

For the second mode, there was a positive charge of 0.41 at E_1 and a negative charge of −1.0 at E_3. The decrease in the charge was clearly visible when combining E_1 and E_3 with $E_{1,3}$ = 0.59. The

FIG. 2. Schematic of the experimental setup for the optical measurement of the cantilever deflection along the cantilever length. The laser beam including the angle of incidence is depicted for a cantilever deflection resulting in a reflected beam hitting the screen at a distance d.
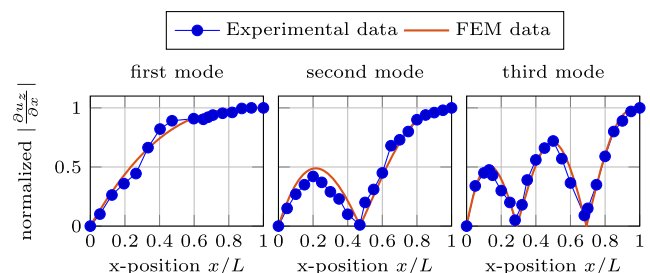
FIG. 3. Optical measurement of cantilever deflection at different positions along the cantilever length for the first three modes at 243 Hz, 1482 Hz, and 4125 Hz. Calculated and measured slopes of the cantilever displacement are given as functions of the cantilever length.
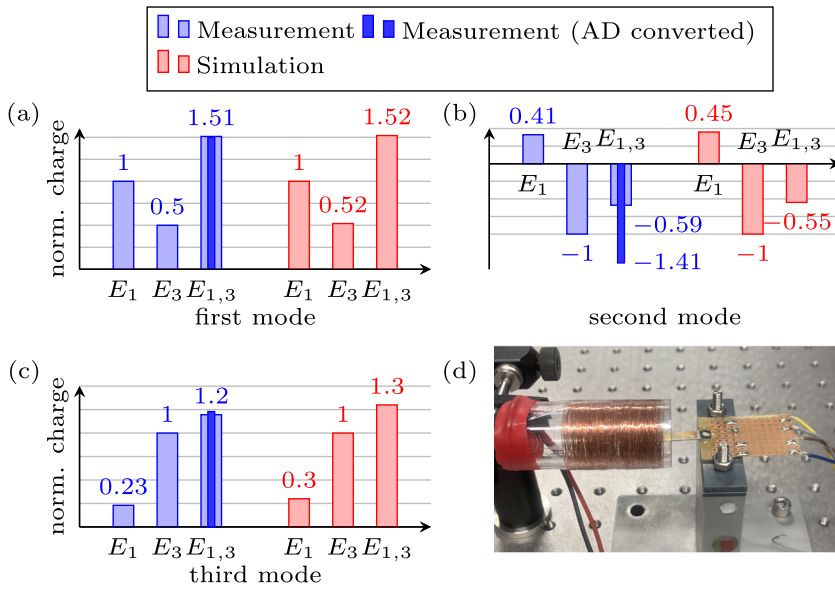
FIG. 4. Normalized charges of different segmented electrodes for the first three modes at 243 Hz, 1482 Hz, and 4125 Hz are shown in (a)–(c). The simultaneous readout of the charges from different electrodes is shown for a direct electrical connection and for a summation after AD conversion. The measurement setup of a cantilever in a coil for magnetic excitation is shown in (d).
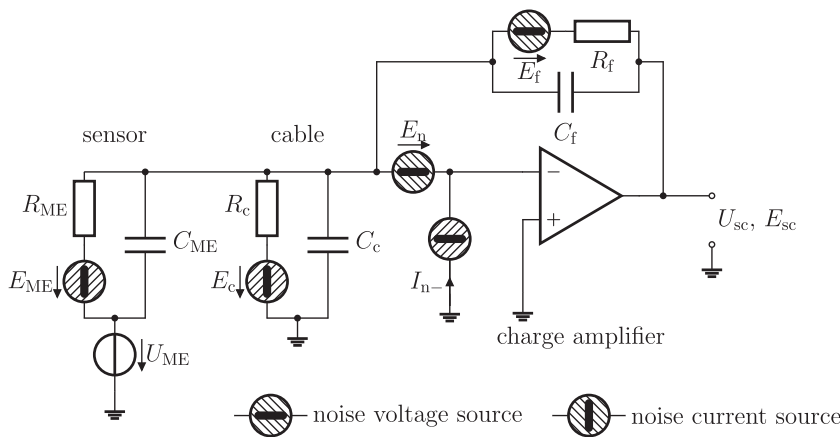

FIG. 5. Equivalent circuit of the sensor and the charge amplifier (based on Jahns et al.[9]). E_{ME} describes the thermal-electrical noise of the piezoelectric phase, E_f is the thermal-electrical noise of the feedback resistor R_f, E_n and I_{n-} are the voltage and current noise of the operational amplifier, and E_c is the thermal-electrical noise of the cable resistance R_c.

digital combination of the electrodes resulted in a much larger charge of −1.41, compared to −0.59, as the signal of E_1 was inverted before the summation. This emphasizes the benefit of summing up the signals in post-processing. For the third mode, the addition of the two positive charges matched the simulation result as well.

As expected, we observed that combining a negatively charged electrode with a positively charged electrode reduces the charge output of the sensor. However, by inverting the output voltage of the charge amplifier and combining the signals afterward, a signal output increase can be achieved. Overall, the experimental data are consistent with the FEM simulation results.

IV. ELECTRODE DESIGN FOR SNR

Using the validated model as described above for the behavior of the cantilever, the electrode design can be adapted to other geometries by calculating the strain node positions and designing the electrodes accordingly. As the signal-to-noise ratio (SNR) is essential for measuring very low magnetic fields, designing the electrodes in terms of optimal SNR can improve the sensor performance.

A. Noise model

To calculate the SNR, not only the signal is required, but also the noise. The noise calculation is done in post-processing using the model developed by Jahns.[9,13] This model includes the Johnson–Nyquist noise of the cantilever and the electronic components, as well as the charge amplifier (AD745) intrinsic noise according to the datasheet. The equivalent circuit of the charge amplifier, the cable, and the sensor is shown in Fig. 5. Although Durdaut et al.[14,15] showed that thermal vibration noise can be the dominant noise source for certain ME sensors, this was not limiting the SNR for

this cantilever. Here, the amplifier voltage noise was the dominant source. To calculate the total noise density at the charge amplifier output, the uncorrelated noise sources of the circuit are added according to Jahns[9,13] (Fig. 5),

$$V_{\text{Noise–SC}} = \left[G_c^2 |Z_{\text{ME}}|^2 \frac{E_{\text{ME}}^2}{R_{\text{ME}}^2} + \left| 1 + \frac{Z_f}{Z_{\text{ME}}} \right|^2 E_n^2 \right.$$
$$+ G_c^2 |Z_{\text{ME}}|^2 I_{n-}^2 + |Z_f|^2 \frac{E_f^2}{R_f^2}$$
$$\left. + |Z_f|^2 \frac{E_c^2}{R_c^2} \right]^{1/2}. \tag{10}$$

Here, $G_c \approx \frac{C_{\text{ME}}}{C_f}$ denotes the charge amplifier gain, $Z_{\text{ME}} = (1/R_{\text{ME}} + i2\pi f C_{\text{ME}})^{-1}$ is the sensor impedance and $Z_f = (1/R_f + i2\pi f C_f)^{-1}$ is the feedback impedance. R_{ME}, R_f, and R_c represent losses in the sensor, the feedback capacitor, and the cable. E_{ME} is the intrinsic electric noise source of the ME sensor, which is given by $E_{\text{ME}} = \sqrt{\frac{4k_B T \tan \delta_{\text{AlN}}}{\omega C_{\text{ME}}}}$, with dissipation factor $\tan \delta_{\text{AlN}} = 0.001$, the Boltzmann constant k_B, and the temperature T. E_f and E_c are the voltage noise densities of the corresponding resistor, which is generally given by $E_R = \sqrt{4k_B T R}$. The cable resistance is $R_c = \frac{1}{\omega C_c \tan \delta_c}$. I_{n-} is the operational amplifier input current noise density, and E_n is the voltage noise density. All noise densities are calculated from the fluctuation–dissipation theorem.[16]

B. Results

The sensor structure investigated in Sec. III was well suited for model validation and principle investigation, but not optimized for high sensitivity. Hence, we decided to analyze the following SNR optimization for a sensor design with much higher sensitivity, which is more suitable for actual measurements. Here, a sensor consisting of a 50 µm thick silicon substrate with a 2 µm thick $(\text{Fe}_{90}\text{Co}_{10})_{78}\text{Si}_{12}\text{B}_{10}$ layer and a 2 µm aluminum nitride layer, a length of 3 mm, and a width of 1 mm was investigated based on sensor structures published in Refs. 6 and 7. The microelectromechanical system (MEMS) fabrication process is described in more detail in Zabel et al.[17] With the signal calculated using the FEM model and the noise calculated in post-processing, the SNR is calculated for different electrode configurations.

As discussed earlier, aligning the electrode positions at the strain nodes results in the highest strain-induced charge because the electrodes cover the largest possible areas with induced charges of equal sign. Nevertheless, for the SNR, shorter electrodes are found to be beneficial. Simply speaking, the charge signal collected close to the strain nodes is very small because there the strain is low, but the collected noise density is constant. Therefore, shortening the electrodes will reduce the collected noise to a higher extent than reducing the signal. To investigate this effect, we varied the electrode start and end positions (x_{start}, x_{end}) for each electrode. As an example, we describe the results and the visualization for electrode E_2 for the third bending mode: The bending mode has an area of constant strain sign between $x_{\text{node, 1}}$ and $x_{\text{node, 2}}$ [Fig. 6(a)]. Accordingly, it can be concluded that the optimization of E_2 is restricted to the interval [$x_{\text{node, 1}}$, $x_{\text{node, 2}}$]. This constrains the possible electrode start and end positions: $x_{\text{start}} \geq x_{\text{node, 1}}$, $x_{\text{end}} \leq x_{\text{node, 2}}$, and $x_{\text{start}} \leq x_{\text{end}}$.
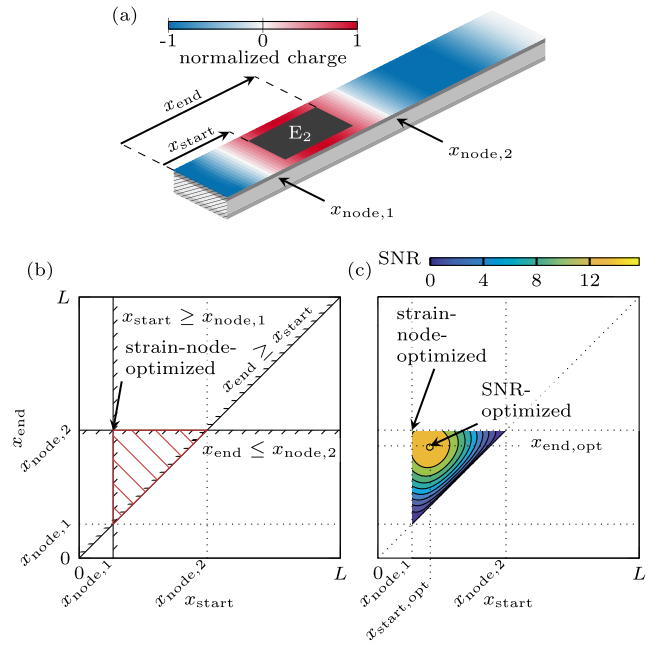

FIG. 6. (a) Cantilever sensor with plotted surface charge density for the third mode. The electrode start x_{start} and end position x_{end} and the strain nodes x_{node} are highlighted for E_2. (b) The red triangle shows exemplarily all possible values for x_{start} and x_{end}, which define the geometry of electrode E_2. The top left corner corresponds to the strain node-optimized electrode (full length electrode). (c) SNR was evaluated for all points of the triangle. The optimum SNR is obtained for a shorter electrode ($x_{\text{node, 1}} < x_{\text{start, opt}}$, $x_{\text{end, opt}} < x_{\text{node, 2}}$). Further details are given in the main text. The optimization results for all modes and electrodes are depicted in Fig. 7.

These conditions are visualized in Fig. 6(b), where the abscissa plots the electrode start position x_{start}, and the ordinate plots the electrode end position x_{end}, resulting in the triangular area (red). The top left corner of the triangle represents the strain node-optimized electrode ($x_{\text{start}} = x_{\text{node, 1}}$, $x_{\text{end}} = x_{\text{node, 2}}$), where the signal is maximal. The opposing hypotenuse represents electrodes of zero length ($x_{\text{start}} = x_{\text{end}}$), resulting in zero signal, hence, zero SNR. The SNRs for the possible electrode configurations of E_2 are plotted in Fig. 6(c) as a two-dimensional color-coded plot, showing an optimum for the marked point ($x_{\text{start, opt}}$, $x_{\text{end, opt}}$). Note that $x_{\text{start, opt}} > x_{\text{node, 1}}$ and $x_{\text{end, opt}} < x_{\text{node, 2}}$. Hence, the optimal electrode configuration has a shorter electrode length compared to the strain-node-optimized configuration.

The results for the remaining bending modes and electrodes are plotted in Fig. 7. For the first mode, the optimal electrode start position is at zero and the end position is at 67% of the cantilever length [Fig. 7(a)]. For the second mode, there are two optimal electrode positions. The first one ends at 15%, and the second one is from 35% to 75% as described above. As expected, there are three optimal electrode positions for the third mode. For the second and third mode, the optimal SNR for each electrode is a local maximum because the SNR is either reduced by altering the start or the end position of the electrode. This dependency is consistent with the one explained for Fig. 6. The SNRs of the higher modes are generally higher compared
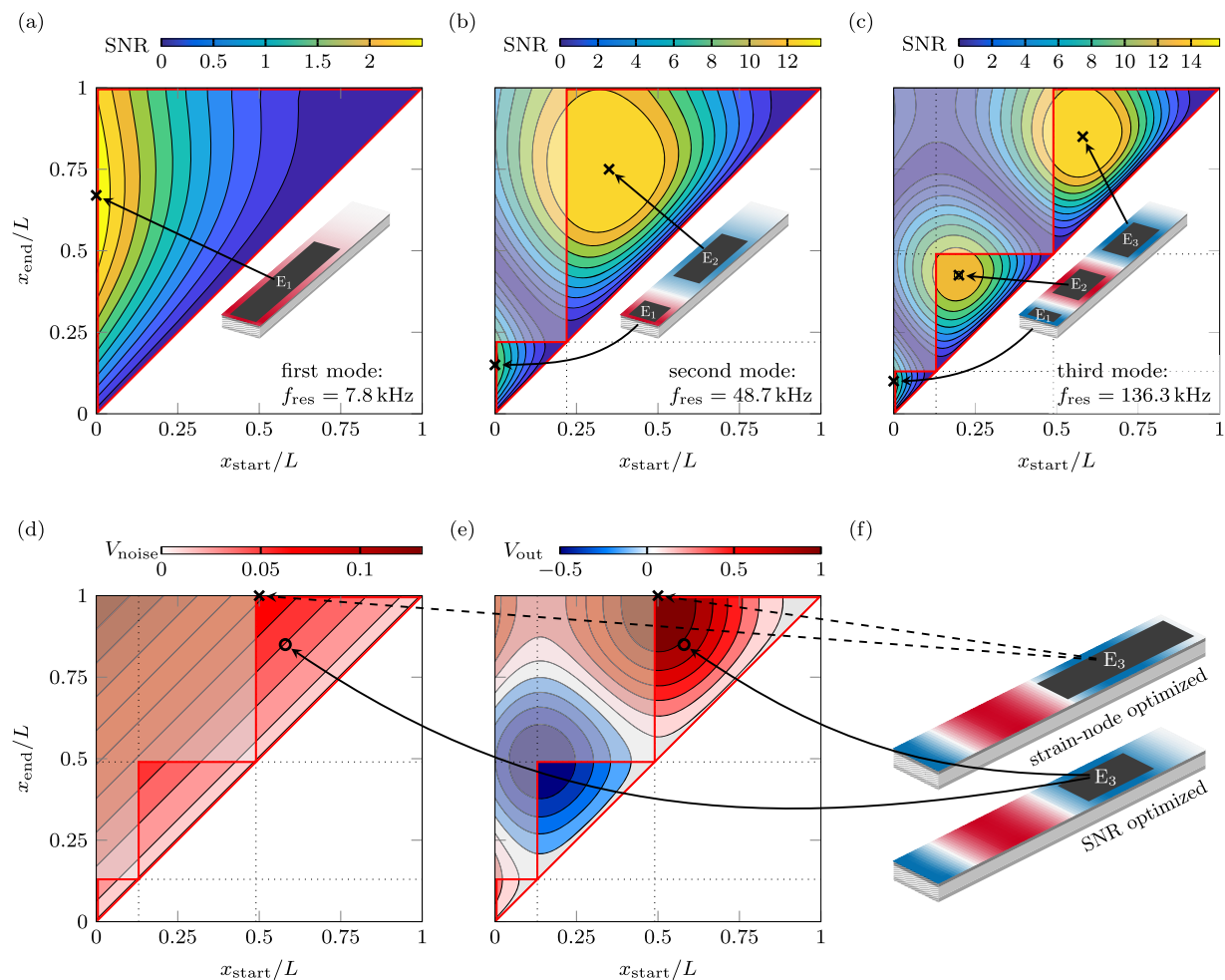
FIG. 7. [(a)–(c)] Signal to noise ratios for different electrode start and end positions along the cantilever length for the first three bound-free bending modes. The insets show cantilevers with the optimal electrode configuration for each mode. The weakly colored areas (top left) correspond to hypothetical electrodes that span over at least one strain node. The noise voltage and output voltage are normalized to the maximum of the output voltage and are shown in (d) and (e), respectively. The crosses and circles indicate the corresponding positions for the strain-node and SNR optimized electrode configurations in the plots. (f) The third electrode for strain-node and SNR optimized configurations. Note that the SNR values are plotted on a linear scale (not in dB).

to the fundamental mode because the noise is reduced with higher frequency by $1/f$ according to Eq. (10). The SNRs are improved by 0.9 dB for the first mode, 2.3 dB for the second mode at electrode E_2, and 2.4 dB for the third bending mode at electrode E_3 compared to full electrodes segmented at strain-nodes. The optimized electrode positions and their signal to noise ratios are summarized in Table I including their gain in SNR compared to a strain-node optimized electrode design.

For all electrodes of higher modes, the SNR is maximized for smaller electrode sizes than the strain-node positions imply. The start and end positions along the cantilever are shifted away from the strain-node positions toward shorter electrode lengths. To give an explicit example that smaller electrode sizes are beneficial for the SNR, the signal and noise voltage are investigated separately [Figs. 7(d) and 7(e)]. The strain-node optimized electrode

configuration for the third mode at electrode E_3 is indicated by a cross in Figs. 7(d) and 7(e), showing the corresponding noise voltage and signal voltage. Compared to the circles indicating the SNR optimized electrode configuration, the signal voltage is reduced by a small amount for the SNR optimized electrode, while the noise voltage is reduced significantly. In this case, the normalized output voltage is reduced by $1 - \frac{0.82\,\text{V}}{1.00\,\text{V}} = 18\%$. However, the noise is reduced by $1 - \frac{0.05\,\text{V}}{0.08\,\text{V}} = 37.5\%$, which gives a higher SNR $\frac{0.82\,\text{V}}{0.05\,\text{V}} / \frac{1.00\,\text{V}}{0.08\,\text{V}} = 1.312 \approx$ 2.4 dB for the electrode configuration with the smaller size. Thus, although the electrodes could be larger without covering the zero stress regions, it is beneficial in terms of greater SNR to have smaller electrodes. This leads to a reduction in the SNR around the optimal electrode configuration as the noise increases more than the signal does with larger electrodes. Enlarging the electrode areas will lower the SNR by increasing noise, but not the signal.

TABLE I. Comparison of the signal-to-noise ratio (SNR) of an electrode configuration optimized by the strain node positions and signal to noise ratio for the first, second, and third modes. ΔSNR shows the improvement by using the SNR optimized electrodes. x_s and x_e describes the electrode start and end position in % of the cantilever length.

	Strain-node optimized			SNR optimized			
	x_s/%	x_e/%	SNR/dB	x_s/%	x_e/%	SNR/dB	ΔSNR/dB
First mode							
E_1	0	100	7.1	0	67	8.0	0.9
Second mode							
E_1	0	22	18.8	0	15	19.4	0.6
E_2	22	100	20.5	35	75	22.8	2.3
Third mode							
E_1	0	13	19.6	0	9	19.9	0.3
E_2	13	49	20.8	20	43	22.2	1.4
E_3	49	100	21.6	58	85	24.0	2.4

V. CONCLUSIONS

Our FEM study shows that the SNR-based design of the electrodes for the analyzed sensor setup improves the higher-mode sensor performance by up to 2.4 dB. This is achieved by reducing the electrode sizes to avoid covering regions with low signal contribution near the strain nodes. In these regions, the noise contribution dominates the signal contribution. The significant improvement shows the importance of this approach for sensing applications, where the maximum SNR is required. The amount of obtained improvement is dependent on the sensor geometry, i.e., length, width, layer heights, chosen materials, and the amplifier. Therefore, the analysis of SNR optimized electrodes has to be adjusted for the design of new or different sensor geometries.

For the readout of a sensor with segmented electrodes, it is possible to hardwire the electrodes of equal polarity for one specific mode. Alternatively, one amplifier for each electrode can be used, combining the amplified electrode signals by operational amplifiers using software-based signal addition after an analog to digital conversion. Another benefit from the second approach is the possibility to do a multi-mode readout of the sensor to further improve the SNR.[6]

Overall, we showed that electrodes designed for optimal SNR can additionally generate sensor improvements and should be considered for applications where the highest sensor performance is desired.

APPENDIX: MATERIAL PARAMETERS

Silicon:[18]

$$c_{Si}^{EH} = \begin{pmatrix} 216 & 84 & 84 & 0 & 0 & 0 \\ 84 & 216 & 84 & 0 & 0 & 0 \\ 84 & 84 & 216 & 0 & 0 & 0 \\ 0 & 0 & 0 & 66 & 0 & 0 \\ 0 & 0 & 0 & 0 & 66 & 0 \\ 0 & 0 & 0 & 0 & 0 & 66 \end{pmatrix} \text{GPa},$$

$$\rho_{Si} = 2329 \, \text{kg/m}^3,$$

$$\varepsilon_{Si} = \begin{pmatrix} 107 & 0 & 0 \\ 0 & 107 & 0 \\ 0 & 0 & 107 \end{pmatrix} \text{pF/m},$$

$$\mu_{Si} = \begin{pmatrix} 0.4\pi & 0 & 0 \\ 0 & 0.4\pi & 0 \\ 0 & 0 & 0.4\pi \end{pmatrix} \mu\text{H/m}.$$

AlN:[18]

$$c_{AlN}^{EH} = \begin{pmatrix} 410 & 149 & 99 & 0 & 0 & 0 \\ 149 & 410 & 99 & 0 & 0 & 0 \\ 99 & 99 & 389 & 0 & 0 & 0 \\ 0 & 0 & 0 & 125 & 0 & 0 \\ 0 & 0 & 0 & 0 & 125 & 0 \\ 0 & 0 & 0 & 0 & 0 & 125 \end{pmatrix} \text{GPa},$$

$$\rho_{AlN} = 3268 \, \text{kg/m}^3,$$

$$\tan \delta_{AlN} = 0.001,$$

$$e_{e,AlN} = \begin{pmatrix} 0 & 0 & 0 & 0 & -0.48 & 0 \\ 0 & 0 & 0 & -0.48 & 0 & 0 \\ -0.58 & -0.58 & 1.55 & 0 & 0 & 0 \end{pmatrix} \text{N/Vm},$$

$$\varepsilon_{AlN} = \begin{pmatrix} 80 & 0 & 0 \\ 0 & 80 & 0 \\ 0 & 0 & 80 \end{pmatrix} \text{pF/m},$$

$$\mu_{AlN} = \begin{pmatrix} 0.4\pi & 0 & 0 \\ 0 & 0.4\pi & 0 \\ 0 & 0 & 0.4\pi \end{pmatrix} \mu\text{H/m}.$$

PVDF–TrFE:[19,20]

$$
\boldsymbol{c}^{\mathrm{EH}}_{\mathrm{PVDF\text{-}TrFE}} = \begin{pmatrix} 4.84 & 2.72 & 2.22 & 0 & 0 & 0 \\ 2.72 & 4.84 & 2.72 & 0 & 0 & 0 \\ 2.72 & 2.72 & 4.63 & 0 & 0 & 0 \\ 0 & 0 & 0 & 0.526 & 0 & 0 \\ 0 & 0 & 0 & 0 & 0.526 & 0 \\ 0 & 0 & 0 & 0 & 0 & 0.526 \end{pmatrix} \mathrm{GPa},
$$

$$
\rho_{\mathrm{PVDF\text{-}TrFE}} = 1879\,\mathrm{kg/m^3},
$$

$$
\tan\delta_{\mathrm{PVDF\text{-}TrFE}} = 0.018,
$$

$$
\boldsymbol{e}_{\mathrm{e,PVDF\text{-}TrFE}} = \begin{pmatrix} 0 & 0 & 0 & 0 & 0.015 & 0 \\ 0 & 0 & 0 & 0.015 & 0 & 0 \\ -4.3 & -4.3 & 0.110 & 0 & 0 & 0 \end{pmatrix} \mathrm{N/Vm},
$$

$$
\boldsymbol{\varepsilon}_{\mathrm{PVDF\text{-}TrFE}} = \begin{pmatrix} 70.84 & 0 & 0 \\ 0 & 70.84 & 0 \\ 0 & 0 & 70.84 \end{pmatrix} \mathrm{pF/m},
$$

$$
\boldsymbol{\mu}_{\mathrm{PVDF\text{-}TrFE}} = \begin{pmatrix} 0.4\pi & 0 & 0 \\ 0 & 0.4\pi & 0 \\ 0 & 0 & 0.4\pi \end{pmatrix} \mathrm{\mu H/m}.
$$

FeCoSiB:[18,21]

$$
\boldsymbol{c}^{\mathrm{EH}}_{\mathrm{FeCoSiB}} = \begin{pmatrix} 150 & 45 & 45 & 0 & 0 & 0 \\ 45 & 150 & 45 & 0 & 0 & 0 \\ 45 & 45 & 150 & 0 & 0 & 0 \\ 0 & 0 & 0 & 40 & 0 & 0 \\ 0 & 0 & 0 & 0 & 40 & 0 \\ 0 & 0 & 0 & 0 & 0 & 40 \end{pmatrix} \mathrm{GPa},
$$

$$
\rho_{\mathrm{FeCoSiB}} = 7250\,\mathrm{kg/m^3},
$$

$$
\boldsymbol{\varepsilon}_{\mathrm{FeCoSiB}} = \begin{pmatrix} 8.854 & 0 & 0 \\ 0 & 8.854 & 0 \\ 0 & 0 & 8.854 \end{pmatrix} \mathrm{pF/m},
$$

$$
\boldsymbol{e}_{\mathrm{m,FeCoSiB}} = \begin{pmatrix} 8500 & -2833.3 & -2833.3 & 0 & 0 & 0 \\ 0 & 0 & 0 & 0 & 0 & 0 \\ 0 & 0 & 0 & 0 & 0 & 0 \end{pmatrix} \mathrm{N/Am},
$$

$$
\boldsymbol{\mu}_{\mathrm{FeCoSiB}} = \begin{pmatrix} 1131 & 0 & 0 \\ 0 & 1131 & 0 \\ 0 & 0 & 1131 \end{pmatrix} \mathrm{\mu H/m}.
$$

DATA AVAILABILITY

The data that support the findings of this study are available from the corresponding author upon reasonable request.

REFERENCES

[1] Y. Zhou, D. J. Apo, and S. Priya, "Dual-phase self-biased magnetoelectric energy harvester," Appl. Phys. Lett. **103**, 192909 (2013).

[2] T.-D. Onuta, Y. Wang, C. J. Long, and I. Takeuchi, "Energy harvesting properties of all-thin-film multiferroic cantilevers," Appl. Phys. Lett. **99**, 203506 (2011).

[3] J. Zhai, Z. Xing, S. Dong, J. Li, and D. Viehland, "Detection of pico-tesla magnetic fields using magneto-electric sensors at room temperature," Appl. Phys. Lett. **88**, 062510 (2006).

[4] J. Petrie, D. Viehland, D. Gray, S. Mandal, G. Sreenivasulu, G. Srinivasan, and A. S. Edelstein, "Enhancing the sensitivity of magnetoelectric sensors by increasing the operating frequency," J. Appl. Phys. **110**, 124506 (2011).

[5] S. Marauska, R. Jahns, C. Kirchhof, M. Claus, E. Quandt, R. Knöchel, and B. Wagner, "Highly sensitive wafer-level packaged MEMS magnetic field sensor based on magnetoelectric composites," Sens. Actuators A: Physical **189**, 321–327 (2013).

[6] J. Reermann, S. Zabel, C. Kirchhof, E. Quandt, F. Faupel, and G. Schmidt, "Adaptive readout schemes for thin-film magnetoelectric sensors based on the delta-E effect," IEEE Sensor. J. **16**, 4891–4900 (2016).

[7] S. Zabel, J. Reermann, S. Fichtner, C. Kirchhof, E. Quandt, B. Wagner, G. Schmidt, and F. Faupel, "Multimode delta-E effect magnetic field sensors with adapted electrodes," Appl. Phys. Lett. **108**, 222401 (2016).

[8] J. L. Gugat, M. C. Krantz, J. Schmalz, and M. Gerken, "Signal-to-noise ratio in cantilever magnetoelectric sensors," IEEE Trans. Magn. **52**, 7005005 (2016).

[9] R. Jahns, R. Knochel, H. Greve, E. Woltermann, E. Lage, and E. Quandt, "Magnetoelectric sensors for biomagnetic measurements," in *2011 IEEE International Symposium on Medical Measurements and Applications* (IEEE, 2011), pp. 107–110.

[10] P. Durdaut, J. Reermann, S. Zabel, C. Kirchhof, E. Quandt, F. Faupel, G. Schmidt, R. Knochel, and M. Hoft, "Modeling and analysis of noise sources for thin-film magnetoelectric sensors based on the delta-E effect," IEEE Trans. Instrum. Meas. **66**, 2771–2779 (2017).

[11] J. F. Blackburn, M. Vopsaroiu, and M. G. Cain, "Verified finite element simulation of multiferroic structures: Solutions for conducting and insulating systems," J. Appl. Phys. **104**, 074104 (2008).

[12] H.-J. Tseng, W.-C. Tian, and W.-J. Wu, "P(VDF-TrFE) polymer-based thin films deposited on stainless steel substrates treated using water dissociation for flexible tactile sensor development," Sensors **13**, 14777–14796 (2013).

[13] R. Jahns, "Untersuchung und optimierung von empfindlichkeit und rauschverhalten magnetoelektrischer sensoren," Ph.D. thesis, 2013, see http://nbn-resolving.de/urn:nbn:de:gbv:8-diss-124422.

[14] P. Durdaut, S. Salzer, J. Reermann, V. Robisch, P. Hayes, A. Piorra, D. Meyners, E. Quandt, G. Schmidt, R. Knochel, and M. Hoft, "Thermal-mechanical noise in resonant thin-film magnetoelectric sensors," IEEE Sensor. J. **17**, 2338–2348 (2017).

[15] M. V. Salapaka, H. S. Bergh, J. Lai, A. Majumdar, and E. McFarland, "Multimode noise analysis of cantilevers for scanning probe microscopy," J. Appl. Phys. **81**, 2480–2487 (1997).

[16] H. B. Callen and T. A. Welton, "Irreversibility and generalized noise," Phys. Rev. **83**, 34–40 (1951).

[17] S. Zabel, C. Kirchhof, E. Yarar, D. Meyners, E. Quandt, and F. Faupel, "Phase modulated magnetoelectric delta-E effect sensor for sub-nano tesla magnetic fields," Appl. Phys. Lett. **107**, 152402 (2015).

[18] J. L. Gugat, M. C. Krantz, and M. Gerken, "Two-dimensional versus three-dimensional finite-element method simulations of cantilever magnetoelectric sensors," IEEE Trans. Magn. **49**, 5287–5293 (2013).

[19] C. W. Nan, M. Li, X. Feng, and S. Yu, "Possible giant magnetoelectric effect of ferromagnetic rare-earth-iron-alloys-filled ferroelectric polymers," Appl. Phys. Lett. **78**, 2527–2529 (2001).

[20] H. Xu, Z.-Y. Cheng, D. Olson, T. Mai, Q. M. Zhang, and G. Kavarnos, "Ferroelectric and electromechanical properties of poly(vinylidene-fluoride-trifluoroethylene-chlorotrifluoroethylene) terpolymer," Appl. Phys. Lett. **78**, 2360–2362 (2001).

[21] A. Ludwig and E. Quandt, "Optimization of the ΔE-effect in thin films and multilayers by magnetic field annealing," in *IEEE International Digest of Technical Papers on Magnetics Conference* (IEEE, 2002) p. AE2.